

# Aberration-corrected Electron Microscopy Imaging for Nanoelectronics Applications

C. Kisielowski<sup>\*,\*\*</sup>, P. Specht<sup>\*\*\*</sup>, D. Alloyeau<sup>\*</sup>, R. Erni<sup>\*</sup>, Q. Ramasse<sup>\*</sup>

*National Center for Electron Microscopy<sup>\*</sup> and Helios SERC<sup>\*\*</sup>, Lawrence Berkeley National Laboratory  
One Cyclotron Road, University of California, Materials Science & Engineering,<sup>\*\*\*</sup> Berkeley CA 94720, USA*

**Abstract.** This paper addresses advances in electron microscopy that were accomplished over the past years with the incorporation of new electron optical components such as aberration correctors, monochromators or high brightness guns. Many of these developments are currently pursued within the DoE's TEAM project. As a result electron microscopy has reached 50 pm resolution. In this paper it is shown how the resolution improvement has helped to boost signal to noise ratios enabling a detection of single atoms across the Periodic Table of Elements. The described achievements allow for investigations of single point defects in nanoelectronic devices even if printed on single sheets of carbon atoms (graphene). Further it is now possible to access depth information from single projections with a precision that has reached interatomic distances.

**Keywords:** Transmission electron microscopy, scanning transmission electron microscopy, image simulation, deep sub Ångstrom resolution

**PACS:** 68.37.Ma, 68.37.Og, 61.05.jd

## INTRODUCTION

Over the past decades atomic resolution electron microscopy steadily evolved by adopting new ideas and new technologies. At the National Center for Electron Microscopy - for example - High Voltage Electron Microscopy was utilized to resolve the atomic structure of materials with ~0.16 nm of lateral resolution in the early 1980s [1]. With the introduction of field emission guns and by merging computer technology and electron microscopy the one Ångstrom barrier was broken in the late 1990s [2] in mid-voltage phase contrast microscopy. Further, a parallel development of pre- and post-specimen aberration correctors [3,4] opened a new route towards deep sub Ångstrom electron microscopy. Currently electron microscopes within DoE's TEAM project [5] are designed around electron optical elements that permit 50 pm resolution in both scanning transmission mode (STEM = Scanning Transmission Electron Microscopy) and broad beam mode (HRTEM = High Resolution Transmission Electron Microscopy). Details about the TEAM 0.5 microscope can be found in reference [6]. In essence, the microscope features a newly developed high brightness gun, a monochromator as well as pre- and

post-specimen Cs correctors. In addition mechanical and electrical stabilities were improved to allow for 50 pm resolution in STEM and TEM modes [7,8].

Since the introduction of atomic resolution electron microscopy, modeling of the scattering and image formation processes was pursued to describe the experiments. In particular multi-slice calculations [9] were very successful in describing quantitatively lattice images obtained in HRTEM mode except for a remaining contrast mismatch [10] that is thought to be of physical or of instrumental nature. Significant progress was made in understanding the image formation in the somewhat more complex STEM mode by adopting and modifying image simulation processes that include scattering to larger angles and a large beam divergence [11].

In fact both imaging modes exhibit intrinsic advantages and the choice of a technique is most commonly dictated by materials properties and research goals. In the particular example of CdS/Cu<sub>2</sub>S nanocrystals shown in Figure 1 much of the desired scientific information is revealed by reconstruction of the electron exit wave function from a focus series of lattice images, which favors HRTEM investigations in this case. However, the situation may be entirely inverted in

other circumstances, where the chemical sensitivity of the High Angle Annular Dark Field imaging (HAADF) mode of STEM can yield invaluable information as illustrated in Figure 2. Here, the  $L1_0$  chemical ordering of multiply twinned magnetic FePt particles is readily observable from the raw images. They also reveal the formation of crystalline rafts of oxidized Fe on the side of certain particles, likely due to the diffusion of Fe from the core of the core-shell icosahedra.

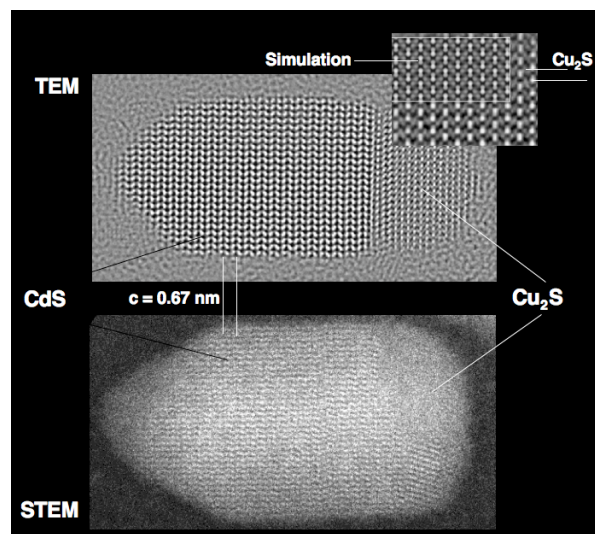


**FIGURE 1.** Experimental STEM (bottom, Z-contrast image) and TEM (top, phase of the reconstructed electron exit wave function) images of CdS/Cu<sub>2</sub>S nanocrystals. Atom columns appear as bright dots in both images. The reconstructed TEM phase image holds much of the desired scientific information such as the crystal structure, a partial copper column occupation, the materials polarity, the interface abruptness or the formation of different phases. Sample: A.P. Alivisatos et al., 2008.

As characteristic length scales of electronic devices approach atomic dimensions, electron microscopy becomes an indispensable characterization tool. We note that there is a seemingly growing belief that the introduction of aberration correctors for HRTEM and STEM largely simplify image interpretation because the atomic materials structure would be directly captured in single images. “Seeing is believing” is a phrase that is sometimes mentioned in this context. Indeed, there are occasions when this view is justified as it applies to samples that are extraordinarily thin such as graphene, which consists of a single layer of carbon atoms [12]. However, such instances are exceptions and nanocrystals of a few nm thickness may already be too thick to allow for direct image interpretation if deep sub Ångström resolution is applied. Therefore, the combination of experiments with simulations will remain a cornerstone for understanding the

underlying science. The science is captured in complex images or image series that remain to be interpreted using image simulations for a verification of the scientific claims.

This paper focuses on methodological aspects of electron microscopy with deep sub Ångström performance. It does not aim at solving a particular materials problem. Instead, the paper elaborates on what is known and expectable from the next generation of electron microscopes by utilizing image simulations as a guideline. It will be shown that the achieved performance improvements open new possibilities for scientific research but also introduce a new set of challenges.

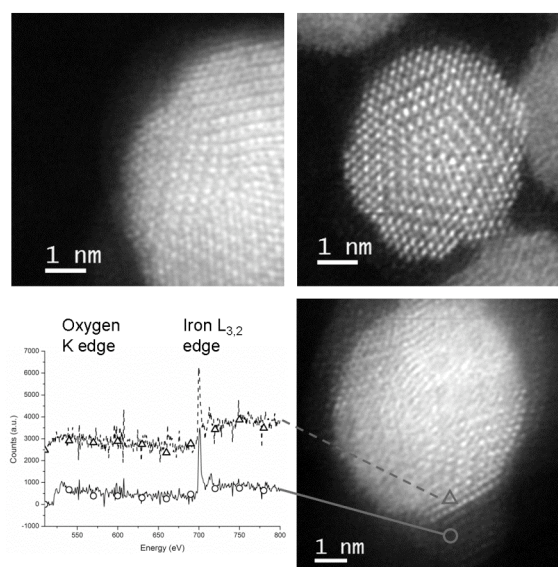


**FIGURE 2.** Experimental Z-contrast STEM images of magnetic FePt nanoparticles. The  $L1_0$  chemical ordering of the multiply twinned Marks decahedra can be readily observed, Pt appearing brighter than Fe in this atomic number Z-sensitive imaging mechanism. The differences between Pt-capped (top right) or Fe-capped (top left) particles is immediately apparent. The formation of crystalline oxidized Fe rafts on the side of the icosahedral core-shell particle, bottom right, is apparent from the image and further revealed by fine probe energy loss analysis. Sample: M. Farle et al., 2007.

Many of the examples given in this paper relate to graphene because of the material’s potential to revolutionize nanoelectronics. In fact, graphene is an example of a material that could allow for the development of electronics on a single sheet of atoms [13]. It is obvious that the material’s characterization requires an adequate resolution of better than 0.14 nm, which is the C-C dumbbell distance in a sheet of graphene. However, it is equally important to obtain signal to noise ratios well above 1 for the detection of single atoms. Thus, it must be a certain combination of resolution and signal to noise ratios that is desired in order

to investigate materials at the single atom level. In the past, the resolution of electron microscopes was sufficient to separate atom columns even if separated by sub Ångstrom values in the projection of an image plane but poor signal to noise levels largely hampered the detection of single light atoms. Therefore, investigations of point defects in semiconductors by electron microscopy were rarely possible.

## ABERRATION CORRECTION

The basic purpose of a microscope is to provide a magnified image of an object, which is not accessible by eye. A one-to-one relation between object and micrograph is thus desirable. Conventional atomic-resolution electron microscopy suffers from the unavoidable spherical and chromatic aberration of round electromagnetic lenses, in particular the aberrations of the magnetic objective lens. While the chromatic aberration essentially affects the information limit of the instrument, in the broad beam HRTEM mode, the spherical aberration imposes a severe restriction on how object information is translated into an image. The spherical aberration leads to a complicated point spread function, which, for instance, explains the image delocalization in conventional HRTEM. This circumstance strongly impairs the interpretability of HRTEM micrographs – independent of specimen thickness. For a rigorous treatment of aberration corrections by hardware see Reference [14].

The Scherzer [15] defocus aims at minimizing the deleterious effect of the inherent lens aberration by counterbalancing the third order spherical aberration against defocus. This enables a broad pass band of direct interpretable image information, approaching the one-to-one relation between image and object. However, atomic resolution information is only interpretable up to the limit imposed by the Scherzer condition, which in the case of field emission transmission electron microscopes is in general significantly smaller than the maximum achievable information transfer.

In conventional high-resolution scanning transmission electron microscopy the effect of the third order spherical aberration of the objective lens is minimized by counterbalancing its effect against defocus (similar to HRTEM) and by limiting the convergence angle of the electron probe. The resulting small probe convergence angle, typically  $\sim 10$  mrad, limits the probe size and the probe current and thus the achievable spatial resolution as well as its use for analytical applications, like electron energy loss spectroscopy (EELS) and energy dispersive X-ray spectroscopy (EDX).

Hence, the spherical aberration of the objective lens imposes severe limits in HRTEM and STEM. While in HRTEM primarily the interpretability of the

micrographs is affected, in STEM it is essentially the resolution. Employing an instrument equipped with a corrector for the spherical aberration, these limitations can be overcome to a large extent. Aberration-corrected electron microscopy has significantly enhanced the interpretability of atomic-resolution HRTEM micrographs. However, owing to the dynamic scattering of the electrons in the specimen, a direct relation between image and object is often absent even for the case of aberration-corrected micrographs. This is particularly true for specimens of thickness  $t > 10$  nm. Sample thickness still prevents a direct relation between a HRTEM micrograph and the corresponding object if the sample thickness is finite. Still, the aberration-corrected optics allow for unambiguously relate the electron wave at the exit plane of the specimen into an image, which is the result of the electron scattering within the specimen. Aberration correction thus simplifies the (optical) point-spread function and makes image interpretation in many respects easier.

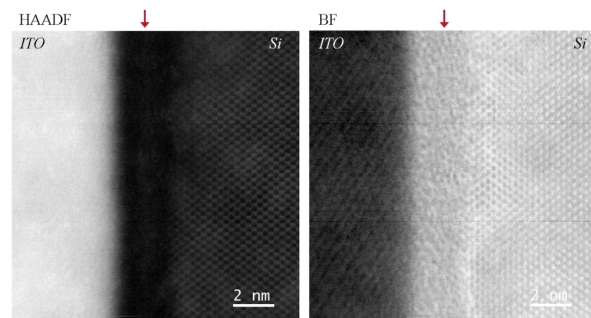


FIGURE 3. Simultaneously acquired HAADF and BF STEM images of a Si/ITO (In-doped tin oxide) interface in a photovoltaic stack. A brighter interlayer (arrow) observed in the HAADF image is not present in the BF image, confirming that the contrast likely arises from the presence of heavier reduced metal [16]. Note also the observable fringes in the BF image, not visible in the HAADF.

The benefits of aberration-corrected probe forming optics in scanning transmission electron microscopy are manifested in smaller electron probes of higher current. This is a direct consequence of the larger beam convergence angle, which can be employed without deleterious effects on the probe shape caused by the spherical aberration. The advantages of aberration-corrected STEM are thus an improved spatial resolution for imaging and a simplified, flexible setup for analytical techniques, which require a large electron dose. For instance, a corollary of the increased convergence angles and currents available in probe corrected instruments is the tremendous improvement in signal collection of bright field (BF) STEM images. The serial nature of the scanning acquisition process and the present beam convergence, however, make

them different from regular HRTEM micrographs. Nevertheless, BF STEM images can generally be collected simultaneously with the HAADF signal, and in conjunction with the latter yield useful additional information such as strain contrast or thickness contrast effects due to extinction distance (Figure 3).

The added flexibility in balancing probe size and probe current with the latest generation of aberration correctors has recently led to the development of low dose techniques aimed at studying extremely beam sensitive materials [17,18] that can require doses as low as 500 electrons/nm<sup>2</sup> in biological applications. Electron doses close to 10000 electrons/nm<sup>2</sup> were recently achieved in STEM through a combination of ultra fast beam scanning, careful selection of optical parameters and emission currents as well as crystallographic processing, whilst preserving preserve atomic resolution information close to the instruments' theoretical resolution.

An important point that needs to be emphasized is that "aberration-corrected" does not mean "aberration-free". An aberration-corrected instrument is free of aberrations to a certain degree or to a certain transfer angle, but is still limited by aberrations, which can be of coherent or incoherent nature. The first generation aberration correctors have essentially aimed at correcting for the third order spherical aberration as well as for potential parasitic axial aberrations up to third order which particularly arise through the implementation of non-round optical elements. This has enabled an aberration free information transfer in HRTEM down to about 0.1 nm and electron probes in STEM of about 0.08 nm at 300 kV. The second generation of aberration correctors, which shall enable even a higher resolution, aims at correcting aberrations up to fifth order. These are thus correctors, which allow for correcting the fifth order spherical aberrations including parasitic axial aberrations up to this order. While the correction of axial aberrations is sufficient to warrant a small aberration-free electron probe, in the case of HRTEM the finite field of view needs to be considered. For a small aberration-corrected electron probe the field that needs to be aberration-corrected is essentially a point-like like object, i.e. the electron probe. For a HRTEM micrograph one expects that the across the field of view the transfer is equivalent – even if not ideal. While axial aberrations lead to a characteristic point spread function reflected, e.g. in the shape of the electron probe, off-axial aberration can lead to apparent image distortions, i.e. the transfer across the field of view is not homogeneous. Hence, apart from correcting axial aberrations, second generation aberration correctors for HRTEM minimize the effect of axial as well as off-axial aberrations.

Complementing the described hardware correction of lens aberrations, the image resolution in HRTEM

can be extended by applying a numerical aberration correction to focal series of lattice images while reconstructing the electron exit wave function. In this manner resolution in HRTEM was extended to reach sub Ångstrom values as early as 2000 using a partly aberration corrected electron microscope [19].

## IMAGE SIMULATIONS

Image simulations are most commonly performed using multislice calculations [9] that can describe well HRTEM and STEM images of electronic devices [20]. A contrast mismatch between calculated and measured phase contrast images is commonly observed that is known as the "Stobbs factor" [10] and influenced by a poor Modulation Transfer Function (MTF) [21, 22] of Charge Coupled Devices (CCD cameras) that are used as detectors.

The visual interpretation of high angle annular dark field images recorded in STEM mode is often considered to be more straightforward than in the case of conventional HRTEM lattice images. By recording electrons scattered to high angles (a typical rule-of-thumb recommending three times the convergence angle for true HAADF) the signal becomes increasingly Rutherford-like and by integrating over an annular detector, the image formation process becomes "incoherent" (i.e. not affected by diffraction interference effects). Further, the recorded intensity is proportional to the  $n$ th power  $Z^n$ ,  $n=1.5-2$ , of the average atomic number  $Z$  of the crystal being observed [23, 24]. HAADF-STEM is therefore often referred to as  $Z$ -contrast imaging (Figure 2). In HRTEM applications the  $Z$  dependence of the image intensity is focus dependent and given by  $\sim Z^{2/3}$  if scattering at single atoms is considered and extraordinary signal to noise ratios can be obtained [25].

Image interpretation can be hindered by the presence of artifacts. For example, the linearity of the relationship between image intensity and chemical composition may break down in HRTEM and STEM images of thick samples and local static displacement fields may cause strain-induced contrast changes [26, 27]. An understanding of such effects requires detailed calculations. J. LeBeau et al. demonstrated recently in the case of SrTiO<sub>3</sub> that  $Z$ -contrast images can be matched quantitatively to simulations, provided that extreme care is taken in characterizing all experimental parameters and that spatial incoherence is taken into account adequately [11]. The absence of a Stobbs factor-like mismatch between simulations and experiment in STEM images points towards a large influence of the detector systems on this debate as recently pointed out for the detection of HRTEM images of thick samples [28]. In case of samples that are only a



few atoms thick, however, the electron beam itself induces atom vibrations that by default must affect any image simulation [29]. In general, STEM simulations require significantly more computation time because of the need to perform a multi-slice calculation at each point of the simulated raster and the present beam convergence

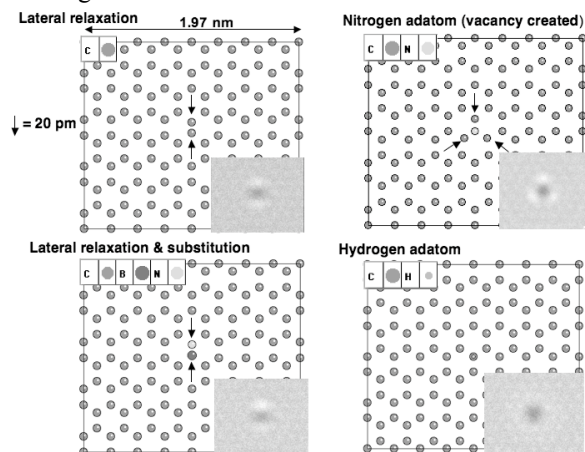


FIGURE 4. Modeling selected point defects (as labeled) in graphene. The insets show multislice phase contrast image calculations for a resolution of 0.3 nm at 100 kV. Arrows mark a 20 pm large displacement of specific atoms. The finite resolution prohibits resolving the atomic defect structure. Nevertheless, all modeled defects create a wide, unstructured signal (insets, dark spots) with  $\sim 0.5\%$  of contrast. A noise level of 0.12 % is assumed.

The necessity to perform detailed numerical simulations also holds true for the interpretation of atomically resolved spectrum images or line profiles, one of the most powerful techniques of the new generation of aberration corrected STEM instruments. Spectrum imaging or EELS linescan techniques are widely accepted to yield atomic resolution information [30] and have been applied to numerous areas of materials research [31-33]. However, one should emphasize that the interpretation of atomically resolved, column-by-column EEL spectra as well as the experimental conditions necessary for their acquisition, are still the subject of ongoing investigations [34-36], where simulations play a major role [37, 38].

In the context of this paper we will primarily consider TEM simulations utilizing multislice calculations that are implemented in the MacTempas software package [39]. Figure 4 depicts four different point defects in a sheet of graphene and their corresponding, calculated Scherzer contrast images at an assumed resolution of 0.3 nm. Atom positions and their chemical identity determine the local phase changes of the scattered electron wave. An additional contrast is generated in the recorded images if single foreign atoms substitute host atoms or if the host atoms are simply displaced by a fraction of the bond length even if atomic resolution is not achieved. Experimentally it

atomic resolution is not achieved. Experimentally it was shown that atom column displacements as small as 2 pm can be observed in phase contract microscopy [40] and it was speculated that even hydrogen atoms may be detectable at a resolution of  $\sim 0.3$  nm [41]. However, the similar contrasts in the images from the very different defects (Figure 5) makes a distinction of different point defects from images with limited resolution ambiguous.

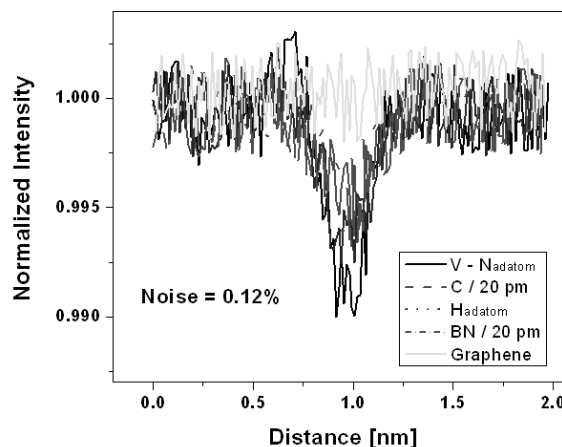


FIGURE 5. Line profiles across the calculated image contrasts for the different defects shown in figure 4. It is seen that the defects are indistinguishable from contrast alone at a noise level of 0.12 %.

## A JUSTIFICATION FOR RESOLUTION IMPROVEMENT

Atomic resolution electron microscopy aims at resolving the atomic structure of materials in order to remove the described ambiguities for image interpretation. Figure 6 depicts Scherzer images of graphene that would be recorded in the TEAM 0.5 microscope and a conventional microscope with 0.3 nm resolution. A resolution enhancement by a factor of 6 seems moderate but it is clear from Figure 6 that its effect on image interpretation is drastic: in case of 0.3 nm resolution the graphene sheet is invisible and the added hydrogen atom is visible as an unstructured contrast that is wider than the atom spacing itself. In contrast, every atom is resolved for the case of 50 pm resolution and it is impressive to see that the space between atoms appears mostly empty. As a result it has become possible to probe for the presence of interstitial atoms [29]. It is further instructive to quantitatively consider the image intensities from Figure 6 by extracting horizontal line traces across the carbon and hydrogen atoms. They are shown in Figure 7. For the case of 0.3 nm resolution the graphene sheet does not produce an intensity pattern but simply a small, homogeneous intensity offset

(< 0.2 %). The hydrogen atom is visible since the signal strength is about 0.5 % and the assumed noise level is only 0.12 %. In contrast, all carbon atoms are visible with a contrast of 8% and a hydrogen atom adds 2% of contrast to the overall signal if the resolution is 50 pm. The 0.12% of noise makes a negligible contribution in this case.

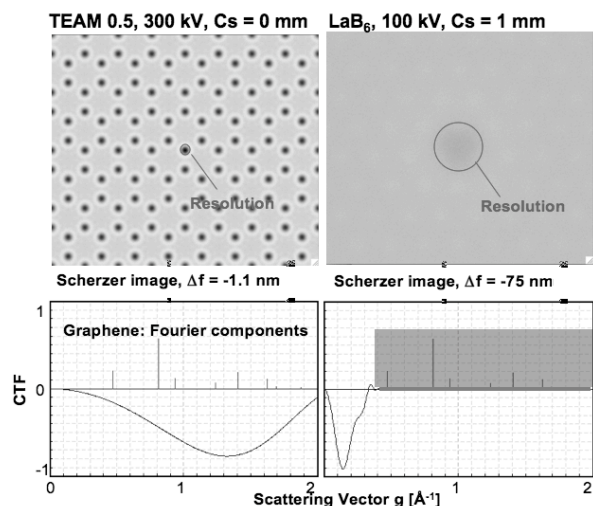


FIGURE 6. Top: Calculated Scherzer images of a graphene sheet with an attached hydrogen atom for the TEAM 0.5 microscope (resolution: 50 pm) and a conventional electron microscope with a resolution of 0.3 nm. Bottom: Corresponding Contrast Transfer Functions with reciprocal lattice vectors ( $g$ ) of graphene. If the CTF equals zero (shaded range) phase information is scrambled and lost.

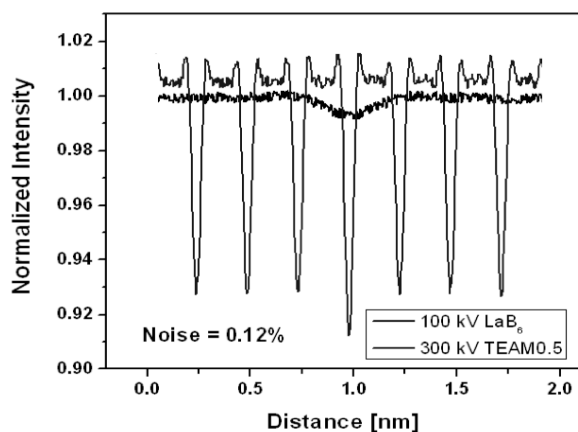


FIGURE 7. Horizontal line profile across the calculated Scherzer images of Figure 6. At the assumed noise level it is in principle possible to detect hydrogen atoms if C-H defects would withstand the necessary e-beam irradiation.

The images of Figure 8 are related experimental examples and they were recorded in the TEAM 0.5 microscope and an environmental Titan (E-TEM) microscope. A single graphene layer together with at-

tached adsorbents was imaged at 80 kV. Successively, an average image pattern and a standard deviation were calculated. The average pattern together with the standard deviation define the signal to noise ratios for the detection of a carbon atom, which are 3.8 and 0.6.

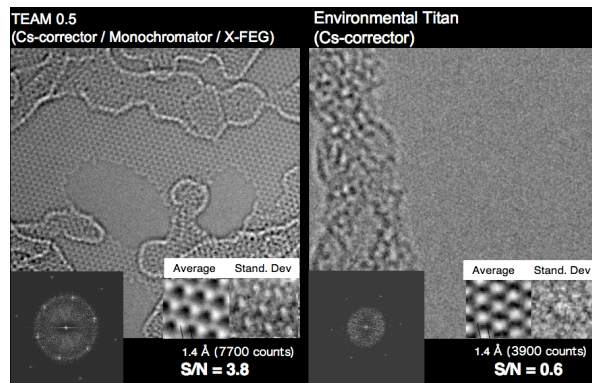


FIGURE 8. Experimental images of a graphene layer. The images were recorded at 80 kV. Two different microscopes are utilized as indicated. Graphene sample: A. Zettl et al. [12]. For details see text.

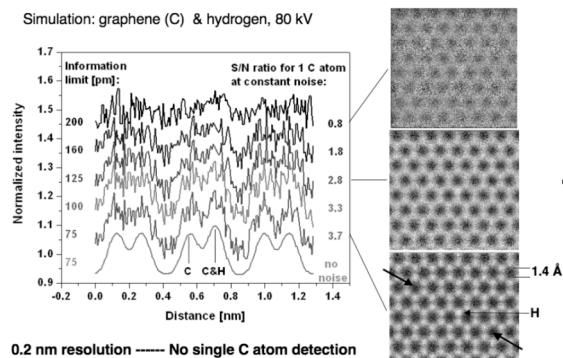


FIGURE 9. Simulations of a hydrogen atom attached to graphene with noise levels that reflect the experimental conditions from Figure 8. Left: line profiles. Right: simulated images. The information limit resolution at 80 kV is varied as indicated.

Since a Cs corrector is employed in both cases the comparison clarifies that it is not the aberration correction itself that yields the resolution and contrast enhancements. Instead, it is the presence of a monochromator and the high brightness gun in TEAM 0.5 that provide a superior image quality by resolution enhancement. Image simulations can be used to estimate the obtained improvement. Figure 9 shows by simulations that a variation of the information limit resolution between 0.2 nm and 0.075 nm yields signal to noise ratios between 0.8 and 3.7 that compare well with the experimental results shown in Figure 8. Therefore, the information limit resolution of TEAM 0.5 is better than one Ångström at 80 kV be-

cause the instrument is equipped with a monochromator and a high brightness gun. However, electron transparent samples are beam sensitive and it is not always possible to further increase the dose in order to boost signal to noise ratios. In fact it seems that the electron dose now limits the resolution in hard materials just as it is the case for electron microscopy of soft materials for a lower dose limit [42].

This example highlights the profound impact of resolution improvement on the ability to detect single atoms and it is desirable to further understand what the physical limits to resolution may be.

## OBJECT-DEFINED RESOLUTION

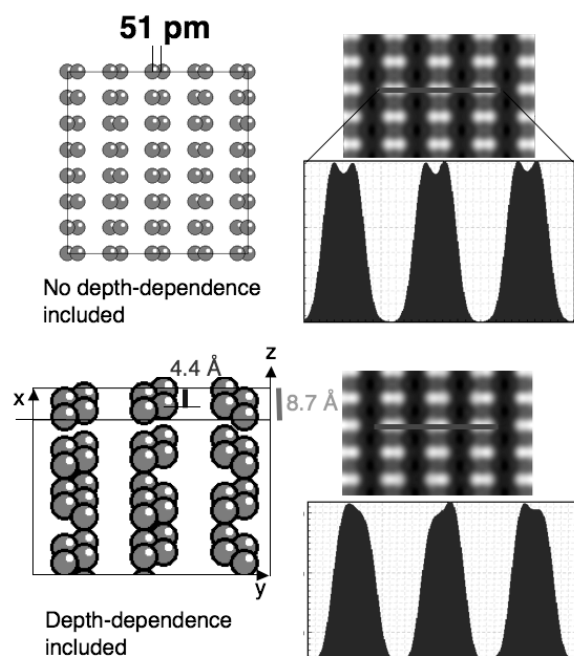


FIGURE 10. Column separation of 51 pm in diamond [112]. Different simulations of a [112] diamond dumbbell structure are employed. Top: The crystal thickness is 0.4 nm and the potential is projected into one plane before calculation. All depth information is lost but a symmetrical dumbbell structure is visible. Bottom: The crystal thickness is 0.89 nm and the potential is sliced to maintain depth information. The dumbbell structure is distorted.

Traditionally established strategies addressing resolution include the recording of Young fringes, the detection of image Fourier components in STEM images, the demonstration of a suitable peak separation in periodic lattices (dumbbell images) or signal width measurements from images of single atoms to name a few procedures. For recent discussions of this topic see references [6, 8, 43, 44]. The drawback of applying different approaches to measure resolution is that the obtained results can differ. Further, it is most common

to define resolution using a selected, suitable sample, in contrast to light microscopy where resolution is instrument-defined. This aspect adds additional uncertainties. In this situation, the TEAM Project adopted the pragmatic view to achieve information transfer below 50 pm by detecting Young fringes in TEM and (660) image Fourier components from gold (111) STEM images at 48 pm. Recently the TEAM 0.5 prototype microscope achieved these goals [6] and resolved dumbbell images of Ge [114] with 47 pm column separation [8].

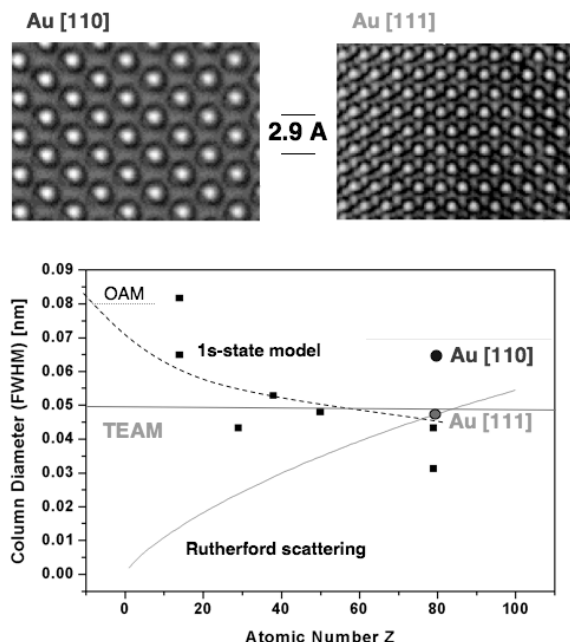


FIGURE 11. Top: Experimental amplitude signal of the channeling wave for gold [110] and [111] recorded in the TEAM microscope. Bottom: Calculated Rutherford scattering cross sections and width of the 1s state. OAM = One Angstrom Microscope [2]. Experimental results are included and compare well with the 1s state theory.

The choice of suitable samples becomes essential if it is attempted to probe for deep sub Ångstrom resolution. For example, using image simulations it was argued that a validation of resolution requires the experimental separation of a suitable dumbbell structure such as it is observable in diamond [112] (Figure 10, top) or other materials along other low index zone axes [45]. On a first glance, such an approach seems reasonable. Nevertheless, the argument is invalid for two reasons: First, it is only possible to calculate symmetrical dumbbell images if all  $z$  (depth) information is removed from the calculation; if depth information is included by an adequate slicing of the unit cell, the dumbbells appear heavily distorted (Figure 10, bottom) because of a present variation of atom positions in beam direction from column to column. Thus,

it is impossible to obtain a symmetrical dumbbell image. Further, even an observation of such distorted dumbbells would require the samples to be extremely thin ( $<1$  nm) because column widths rapidly increase with sample thickness yielding a broad unresolved signal in TEM [2]. It would be quite challenging if not impossible to prepare electron transparent samples in the desired crystallographic orientation that are only one or two atoms thick.

The rapid column broadening with sample thickness can be understood physically in the framework of electron channeling [46]: Two extreme physical limits to resolution are depicted in the graph of Figure 11. In the one extreme, electron channeling dominates yielding a finite column width [47,48] and in the other extreme it is the cross section for Rutherford scattering at single atoms [49]. The channeling model predicts that a resolution well below 80 pm cannot be obtained if columns of light elements are imaged. On the other hand, resolution tests using heavy elements with  $Z \sim 80$  are less critical since both models converge for heavy atoms and both models allow for 50 pm resolution. Therefore, the TEAM project used gold ( $Z=79$ ) crystals to probe for the object-defined resolution.

Figure 11 also shows two amplitude images of electron channeling waves that were reconstructed from  $\sim 20$  experimentally recorded lattice images of gold crystals imaged in [110] and [111] direction. In  $z$  (beam) direction, the gold atoms are spaced by 0.29 nm in [110] projection but are 0.7 nm apart in [111] projected samples. The atom spacing in beam direction alters electron channeling significantly. It is seen from the images shown in Figure 11 that atom columns appear much wider in [110] projection at comparable sample thicknesses (the full width at half maximum of the white blobs is  $67 \pm 4$  pm and  $46 \pm 3$  pm in Au [110] and Au [111], respectively, at a sample thickness of  $5 \pm 1$  nm [7]). It is seen that theory and experiment agree decently well; in particular column widths are expected to be wider in gold [110], which cannot be used to verify a resolution of 50 pm in contrast to gold [111].

The results are consistent with predictions from multislice calculations and also observable in HAADF STEM images from Au [110] and Au [111]. Therefore, the TEAM 0.5 microscope can resolve column spaced as narrow as 50 pm if the samples are carefully chosen and prepared. In general, however, electron channeling limits the resolution of electron microscopes to values between 80 pm and 50 pm depending on the atomic number  $Z$  and the spacing of atoms in beam direction. Thus, the TEAM microscope has reached a resolution that is limited by physical limits of electron scattering.

## DEPTH PRECISION

A resolution of 50 pm implies a focus spread of the electron beam of only 0.7 nm in TEM mode [6]. For comparison, focus spread values in TEMs with  $\sim 0.2$  nm resolution are commonly 5 nm. Such unprecedented small focus spread values enable new experiments.

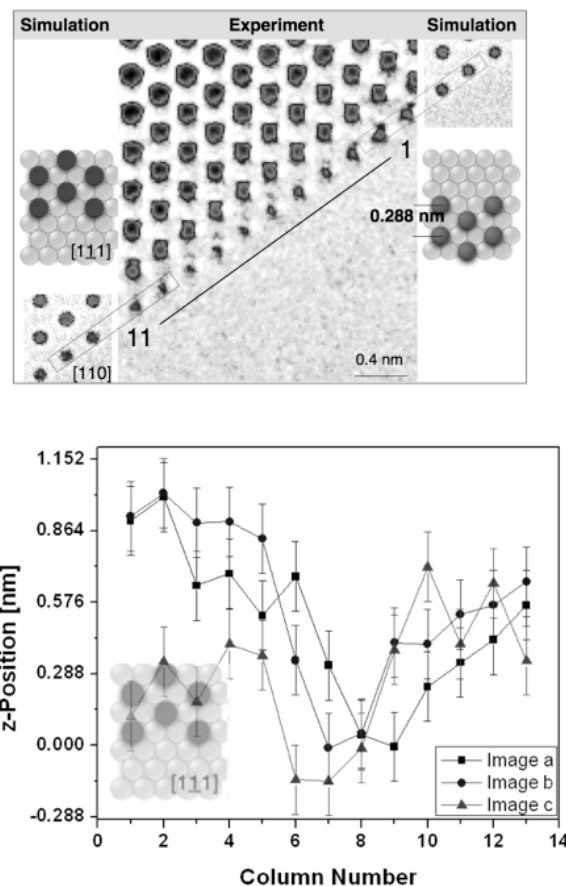


FIGURE 12. Top: Experimental and simulated lattice image of a gold bridge. All images are shown in [110] projection, the geometrical models are shown in the perpendicular [111] projection. Atom columns 1- 11 contain 2 atoms each [6]. 3% noise is included. Bottom: Quantitative conversion of contrast values into  $z$ -positions from 3 successive lattice images. In the fourth image columns 1 -7 escape observation by knock on damage [6]. Image b is shown in the figure.

It was recently pointed out for instance that atom displacements in the beam direction as small as interatomic distances can now be detected because related focus changes of  $\sim 0.2$  nm already yield contrast variations in the images above noise levels [6]. Likewise in STEM, aberration correctors can now control aberrations up to 35 mrad away from the optic axis. Such large convergence angles imply that the electron probe is now typically only focused in a 2-3 nm section through the depth of the specimen (along the beam



direction), compared to tens of nm for non-corrected instruments [50]. By depth slicing through the observed sample, it is now possible to reveal buried defects and thus allow for recovering some three-dimensional information from a single projection image [6, 50, 51].

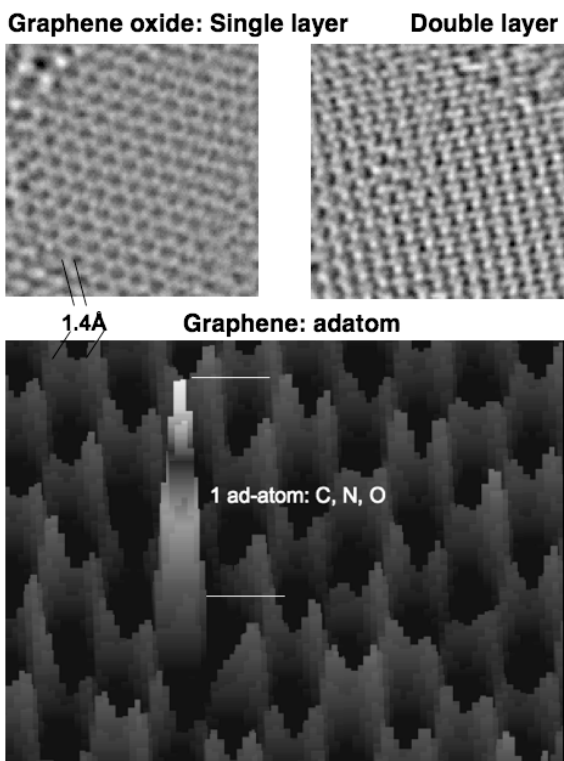


FIGURE 13. Phase of the electron exit wave function reconstructed from series of experimental lattice images of graphene oxide & graphene. Top: Graphene oxide is inhomogeneous but single and double layers can be recognized locally. Bottom: A single light atom (shaded) is attached to a graphene sheet (dark gray) and generates a signal that exceeds largely the present noise level. Graphene sample: A. Zettl et al. [12]. Graphene oxide sample: J.H. Blackson.

An experiment that exploits depth precision is shown in Figure 12. The depicted lattice image is taken from a published focus series of a gold bridge [6] and compared with image simulations. We focus the contrast analyzes on a row of atom columns at the crystal-vacuum interface that contain 2 atoms each. All columns are attached to a narrow crystal facet that is only about 1 nm tall. Contrast is converted to z-position for each of the 2-atom columns and displayed in Figure 12. The procedure is repeated for 3 successive lattice images that could be recorded before the considered row of 2 atom columns disintegrates because of knock on damage. It is seen that experimental data can be reproduced well within experimental errors of  $\sim 0.3$  nm. The z-difference between columns 1 and 11 equals the smallest 0.288 nm displacements of atom

columns in z-direction that is imposed by the [110] crystal structure. This minimal displacement is directly visible in the lattice image because the noise is only 3% as demonstrated by comparing the experiment with simulations. Further, 3D information is recovered by showing that the atom row is bent in a V-shaped manner.

Nowadays, nanoelectronics applications often focus on exploiting physical properties of graphene. In Figure 13 we used graphene oxide and a single graphene layer [12] to demonstrate that single and double layers can be readily imaged and that an attached single light atom can indeed be detected well above noise, which allows studying doping effects or functionalization. Single atom sensitivity is a further step towards atomic resolution electron tomography [52].

## CONCLUSIONS

This paper summarizes some new, largely unexplored capabilities of electron microscopy that become possible because of aberration correction and the development of new electron optical hardware components. Outstanding aspects of electron microscopy with deep sub Ångström resolution are the ability to detect single atoms across the Periodic Table of Elements and the possibility to recover depth (z) information from single projections with a precision that approaches interatomic distances. Resolution has reached 50 pm and is now limited by the electron scattering process in the samples. Atomic resolution can be achieved for acceleration voltages between 80 and 300 kV. The electron dose and physical aspects of electron scattering limit the obtainable image (object) resolution now.

## ACKNOWLEDGMENTS

The TEAM project is supported by the Department of Energy, Office of Science, Office of Basic Energy Sciences. NCEM is supported by the Department of Energy, Contract # DE-AC02-05CH11231. E-TEM images were recorded for Helios SERC at CEN-DTU with kind support of R. Dunin-Borkowski and J. Jinschek.

## REFERENCES

1. D.J. Smith, R.A. Camps, L.A. Freeman, M.A. O'Keefe, W.O. Saxton, G.J. Wood, *Ultramicroscopy*, **18**, 63-76, (1985).
2. C. Kisielowski, C.J.D. Hetherington, Y.C. Wang, R. Kilaas, M.A. O'Keefe, A. Thust, *Ultramicroscopy*, **89**, 243-263 (2001).
3. M. Haider, S. Uhlemann, E. Schwan, H. Rose, B. Kabius, K. Urban, *Nature* **392**, 768-769 (1998).

4. P.D. Nellist, M.F. Chisholm, N. Dellby, O.L. Krivanek, M.F. Murfitt, Z.S. Szilagyi, A.R. Lupini, A. Borisevich, W.H. Sides, S.J. Pennycook, *Science* **305**, 1741 (2004).
5. <http://ncem.lbl.gov/team/TEAMpage/TEAMpage.html>
6. C. Kisielowski, B. Freitag, M. Bischoff, H. van Lin, S. Lazar, G. Knippels, P. Tiemeijer, M. van der Stam, S. von Harrach, M. Stekelenburg, M. Haider, H. Muller, P. Hartel, B. Kabius, D. Miller, I. Petrov, E. Olson, T. Donchev, E.A. Kenik, A. Lupini, J. Bentley, S. Pennycook, A.M. Minor, A.K. Schmid, T. Duden, V. Radmilovic, Q. Ramasse, R. Erni, M. Watanabe, E. Stach, P. Denes, U. Dahmen, *Microscopy and Microanalysis* **14**, 454-462 (2008).
7. C. Kisielowski, R. Erni, B. Freitag, *Microscopy and Microanalysis* **14** Suppl. 2, 78-79 (2008).
8. R. Erni, M.D. Rossell, C. Kisielowski, U. Dahmen, *Phys. Rev. Lett.* **102**, 096101 (2009).
9. J.M. Cowley, A.F. Moodie, *Acta Cryst.* **10**, 609-619 (1957).
10. M.J. Hytch and W.M. Stobbs, *Ultramicroscopy* **53**, 191 (1994).
11. J.M. LeBeau, S.D. Findlay, L.J. Allen, S. Stemmer, *Phys. Rev. Lett.* **100**, 206101 (2008).
12. Çağlar Ö. Girit Jannik C. Meyer, Rolf Erni, Marta D. Rossell, C. Kisielowski, Li Yang, Cheol-Hwan Park, M. F. Crommie, Marvin L. Cohen, Steven G. Louie, A. Zettl, *Science* **323**, 1705 (2009).
13. F. Wang, Y. Zhang, C. Tian, C. Girit, A. Zettl, M. Crommie, Y. Ron Shen, *Science* **320**, 206 (2008).
14. H. Rose, Geometrical Charged-Particle Optics, Springer series in optical sciences 142, Berlin (2009).
15. O. Scherzer, *Z Phys* **101**, 593-603 (1936).
16. Q.M. Ramasse, A. Anapolsky, C. Lazik, M. Jin, K. Armstrong and D. Wang, *Journal of Applied Physics* **105**, 033716 (2009).
17. J.E. Evans, C. Hetherington, A. Kirkland, L.-Y. Chang, H. Stahlberg and N.D. Browning, *Ultramicroscopy* **108**, 1636-1644 (2008).
18. J.P. Buban, Q.M. Ramasse, B. Gibson, N.D. Browning and H. Stahlberg, *Submitted* (2009).
19. C. Kisielowski, E.C. Nelson, C. Song, R. Kilaas, A. Thust, *Microscopy and Microanalysis* **6**, Sub. 2, 16 (2000).
20. A. C. Diebold B. Foran, C. Kisielowski D. Muller S. Pennycook E. Principe S. Stemmer, *Microscopy and Microanalysis* **9**, 493-508 (2003).
21. M.A. O'Keefe, C.J.D. Hetherington, Y.C. Wang, E.C. Nelson, J.H. Turner, C. Kisielowski, J.-O. Malm, R. Mueller, J. Ringnalda, M. Pam, A. Thust, *Ultramicroscopy* **89**, 215 (2001).
22. C. Dwyer, R. Erni and J. Etheridge, *Applied Physics Letters* **93**, 021115 (2008).
23. P. Hartel, H. Rose and C. Dinges, *Ultramicroscopy* **63**, 93-114 (1996).
24. D. Jesson and S.J. Pennycook, *Proceedings of the Royal Society of London A* **449**, 273-293 (1995).
25. J.R. Jinschek, C. Kisielowski, D. Van Dyck, P. Geuens, *SPIE* **5187**, 54 (2004).
26. S. Hillyard, J. Silcox, *Ultramicroscopy* **58**, 6-17 (1995).
27. M. Herrera, Q.M. Ramasse, N.D. Browning, J. Pizarro, D. Gonzalez, R. Garcia, M.W. Du, S.B. Zhang and M. Hopkinson, "Analysis of the mechanism of N incorporation in N-doped GaAs quantum wells", in *EMC 2008, Vol. 1: Instrumentations and Methods*, edited by M. Luysberg, K. Tillmann and T. Weirich, Springer-Verlag (2008), pp. 3-4.
28. A. Thust, M. Luysberg, K. Tillmann, T. Weirich (Eds.): *EMC 2008, Vol. 1: Instrumentation and Methods*, pp. 163-64,
29. D. Alloyeau, B. Freitag, S. Dag<sup>3</sup>, Lin W. Wang, C. Kisielowski, *Phys. Rev. B* (2009), in press
30. R.F. Klie, I. Arslan and N.D. Browning, *Journal of Electron Spectroscopy and Related Phenomena* **143**, 105-115 (2005).
31. J.C. Loudon, L.F. Kourkoutis, L.F. Ahn, C.L. Zhang, S.W. Cheong and D.A. Muller, *Physical Review Letters* **99**, 237205 (2007).
32. M. Varela, T.J. Pennycook, W. Tian, D. Mandrus, S.J. Pennycook, V. Pena, Z. Sefrioui and J. Santamaria, *Journal of Materials Science* **41**, 4389 (2006).
33. G. Yang, Q.M. Ramasse and R.F. Klie, *Physical Review B* **78**, 153109 (2008).
34. L.J. Allen, S.D. Findlay, A.R. Lupini, M.P. Oxley and S.J. Pennycook, *Physical Review B* **76**, 034303 (2003).
35. D.A. Muller, L. Fitting, S. Thiel, A. Schmehl and J. Mannhart, *Ultramicroscopy* **106**, 1053-1061 (2006).
36. M. Bosman, V. Keast, J.L. Garcia-Munoz, A.J. D'Alfonso, S.D. Findlay and L.J. Allen, *Physical Review Letters* **99**, 086102 (2007).
37. C. Dwyer, S.D. Findlay and L.J. Allen, *Physical Review B* **77**, 184107 (2008).
38. J. Verbeeck, P. Schattschneider and A. Rosenauer, *Ultramicroscopy* **109**, 350-360 (2009).
39. <http://www.totalresolution.com/>
40. X. Xu, S.P. Beckman, P. Specht, E.R. Weber, D.C. Chrzan, R. P. Erni, I. Arslan, N. Browning, A. Bleloch, C. Kisielowski, *Phys. Rev. Lett.* **95**, 145501 (2005).
41. J. C. Meyer, C. O. Girit, M. F. Crommie, A. Zettl, *Nature* **454**, 319-322 (2008).
42. C. Kisielowski, R. Erni, J. Meyer, *Imaging & Microscopy* **10**, 24-25 (2008)
43. Y. Peng, M.P. Oxley, A.R. Lupini, M.F. Chisholm, S.J. Pennycook, *Microsc Microanal* **14**, 36-47 (2008).
44. A.J. den Dekker, A. van den Bos, *J Opt Soc Am A* **14**, 547-557 (1997).
45. M.A. O'Keefe, *Ultramicroscopy*, **108** (3), 196-20 (2008)
46. S. Van Aert, P. Geuens, D. Van Dyck, C. Kisielowski, J.R. Jinschek, *Ultramicroscopy* **107**, 551-8 (2007).
47. A.J. den Dekker, S. Van Aert, D. Van Dyck, A. Van der Bos, P. Geuens, *Ultramicroscopy* **89**, 275 (2001).
48. S. Van Aert, A.J. den Dekker, D. Van Dyck, A. van den Bos, *Ultramicroscopy* **90**, 273 (2002)
49. L. Reimer, Transmission Electron Microscopy, Springer, Optical Sciences, Berlin 1993, p. 152.
50. H.L. Lin, V. Intaraprasong, D.A. Muller, *Applied Physics Letters* **92**, 013125 (2008).
51. K. van Benthem, A.R. Lupini, M.P. Oxley and S.J. Pennycook, *Ultramicroscopy* **106**, 1062-1068 (2006).
52. J.R. Jinschek, K.J. Batenburg, H.A. Calderon, R. Kilaas, V. Radmilovic, C. Kisielowski, *Ultramicroscopy* **108**, 589-604 (2008).